This is the Pre-Published Version.

Journal Name

ARTICLE

Disordered Layers on WO_3 Nanoparticles Enable Photochemical Generation of Hydrogen from Water

Received 00th January 20xx,
Accepted 00th January 20xx

DOI: 10.1039/x0xx00000x

www.rsc.org/

Luyang Wang,[a] Chui-Shan Tsang,[a] Wei Liu,[a] Xiandi Zhang,[a] Kan Zhang,[b] Enna Ha,[a] Wai-Ming Kwok,[a] Jong Hyeok Park,[b] Lawrence Yoon Suk Lee,[*a] and Kwok-Yin Wong[*a]

Tailored defects on semiconductor surface can provide active catalytic sites and effectively tune the electronic structure for suitable optical properties. Herein, we report that surface modification of WO_3 with disordered layer enables the photochemical hydrogen production from water. A simple room temperature solution process with lithium-ethylenediamine (Li-EDA) alters the surface of WO_3 with localized defects that form a thin disordered layer. Both structural and optical characterizations reveal that such disordered layer induces an upshift in Fermi level and the elevation of the conduction band of WO_3 above the hydrogen reduction potential. Using alkaline sacrificial agent, Li-EDA treated WO_3 shows a co-catalyst-free photochemical hydrogen evolution rate of 94.2 μmol g^{-1} h^{-1} under simulated sun light. To the best of our knowledge, this is the first example of WO_3 as a direct photocatalyst for hydrogen generation from water via simple surface defect engineering.

Introduction

Solar energy-driven hydrogen generation from water can offer a clean and sustainable solution to address the growing energy demand with reduced fossil fuel dependence and associated environmental issues.[1-3] In recent years, much effort has been made to develop effective photocatalysts based on abundant and economic elements.[4-7] However, their overall photocatalytic efficiencies are insufficient to replace those made of noble metals. Tuning the light absorption, charge kinetics, and surface activity of catalysts can elevate the photocatalytic performance, but it is still challenging to achieve the activity of noble metal-based ones.

Semiconductor metal oxides, with advantages of natural abundance, chemical stability, and low cost, have been widely used as photocatalysts and electrode materials for energy conversion and storage devices.[8] Both electronic and optical properties of metal oxides can be regulated by the type and population of defect introduced. The creation of intrinsic defects, such as oxygen vacancies and doping of low valence metal centers or non-metal atoms, are the most commonly used defect engineering methods for tailoring the photocatalytic activity.[9-12] In particular, oxygen vacancies are known to serve as shallow donors for metal oxides, such as TiO_2,[13] WO_3,[14] and SnO_2.[15] It is generally accepted that the increased carrier density improves the electrical conductivity and facilitates the charge transfer at the interface between metal oxide and substrate.

The introduced defects can be extended to form an internal boundary[7] or even disordered layer,[10] which are relatively less studied than atomic point defects. Surface disordered layer arises from the large amount of lattice disorder on the crystalline surface after being treated under reducing conditions. Such layers usually contain a significant amount of oxygen vacancies and the low valence metal centers (self-doped), which may create the mid-gap states below the Fermi level of the metal oxide.[16] The mid-gap states form a continuum that extends to and overlaps with the conduction band (CB) or merges with the valence band (VB). This can effectively reduce the band gap and enhance the light absorption in visible and near-IR regions.[17, 18] These extended energy states and the newly produced energy levels may become dominant for optical excitation and relaxation, and thus new application may be endowed. Furthermore, the localized holes generated in the mid-gap state of the disordered layer efficiently inhibit the charge recombination,[16, 19-22] where the low valence metal centers act as a trapping sites for photogenerated carriers.

The pioneering work of black TiO_2 with disordered surface layers[16] demonstrated a significant enhancement in photocatalytic hydrogen evolution reaction (HER) rate and has sparked the investigations of creating disordered layer in other metal oxides, including Fe_2O_3,[23] ZnO,[24] $BiVO_4$,[25] and WO_3.[26, 27] Among them, tungsten oxide (WO_3) is an important *n*-type semiconductor of various applications ranging from dye-sensitized solar cell[28] to electrochromic devices,[29] gas sensors,[30] and photoelectrochemical water splitting,[31] owing to low cost and good conductivity. With the desirable bandgap energy (2.5–2.8 eV) for capturing visible light and a number of stable oxygen-deficient sub-stoichiometric structures (WO_{3-x}, where $0 < x \leq 0.28$) available, WO_3 is one of the most attractive candidates for photocatalytic water splitting.[32] Nonetheless, restricted by its intrinsic electronic structure, WO_3 is only suitable for water oxidation.[33] The positon of valence band maximum (VBM) of WO_3 is located at a relatively high energy level (3.0 eV *vs.*

[a] *Department of Applied Biology and Chemical Technology and the State Key Laboratory of Chemical Biology and Drug Discovery, The Hong Kong Polytechnic University, Hung Hom, Hong Kong SAR, China.*
[b] *Department of Chemical and Biomolecular Engineering, Yonsei University, 50 Yonsei-ro, Seodaemun-gu, Seoul 120-749, Republic of Korea.*

† Electronic Supplementary Information (ESI) available: See DOI: 10.1039/x0xx00000x

reversible hydrogen electrode, RHE), whereas the conduction band minimum (CBM) lies at a position lower than hydrogen reduction potential (0 V *vs*. RHE).

Recently, thin disordered layer on WO_3 surface has been reported to significantly increase the charge carrier density and facilitate the interface charge transfer, thus improve the charge separation efficiency and conductivity in photoelectrocatalytic water oxidation.[26, 27] Localized surface atomic disorder was also engaged to turn the inert WO_3 to an active electrocatalyst for hydrogen generation from acidic water.[34] Nevertheless, it is still challenging to trigger solar water reduction using WO_3 and the effect of surface disordered layer on the band structure of WO_3 has not been clearly understood yet. Herein, we demonstrate that a simple room-temperature solution processing method can modify the surface morphology and electronic structure of WO_3 to enable the unprecedented capability of photocatalytic HER without co-catalyst. Using Li-ethylenediamine (Li-EDA) as a disordering agent, surface disordered layer was successfully created on the crystalline WO_3 nanoplates (see Scheme 1 for synthetic schematics). Experimental results confirm the formation of mid-gap state that causes the blue-shift in both CBM and Fermi level (E_f) with respect to pristine WO_3. The reformed band structure of Li-EDA treated WO_3 (LT-WO_3) allows the photocatalytic hydrogen evolution without the assistance of co-catalyst at a steady rate of 94.2 μmol g^{-1} h^{-1} under simulated sun light. With the first example of using WO_3 as a co-catalyst-free photocatalyst for HER, we demonstrate that Li-EDA treatment can be applied as a simple yet effective strategy to tailor the optical band structure of metal oxide *via* the formation of thin disordered surface layer.

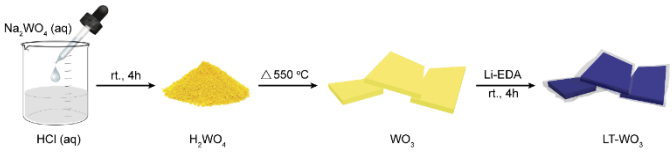

Scheme 1. Schematic illustration of synthetic procedure for WO_3 with surface disordered layer (LT-WO_3).

EXPERIMENTAL SECTION

Synthesis of WO_3 nanoplates.

Sodium tungstate solution (0.4 mol L^{-1}) was added to excess hydrochloric acid solution (1 mol L^{-1}) under vigorous stirring to obtain the tungstic acid nanoparticle precipitate. The yellow precipitate was collected after centrifugation, and washed with water for 3 times. Afterwards, the as-prepared solids were calcinated at 550 °C under Ar atmosphere for 3 h. The product was collected after the furnace cooled down to room temperature.

Synthesis of LT-WO3 nanoplates.

The as-synthesized WO_3 nanoplate was immersed into the solvated electrons solution, Li-EDA (1 mol L^{-1}), at room temperature with continuous stirring for 4 hours. After quenching the reaction with deionized water, the resulting dark blue precipitate was collected using centrifugation. The solids were washed with HCl solution (0.5 mol L^{-1}) and ethanol alternately in order to remove any physically adsorbed Li and EDA. It was then dried under vacuum at room temperature overnight.

Photocatalytic H_2 production.

In a typical run, 5 mg sample was suspended in a 25 mL mixture solution of Na_2S (0.35 M) and Na_2SO_3 (0.25 M). The solution was degassed with N_2 for 30 minutes. Afterwards, the as-prepared solution was irradiated with a Newport solar simulator (150 W Xe lamp, ozone free, Air Mass Filter, AM 1.5 Global) of 100 mW cm^{-2} light intensity under stirring. The amount of generated H_2 was analyzed by an Agilent 7890B gas chromatograph system equipped with a TCD detector using N_2 as carrier gas.

Sample characterization.

The crystal structure of samples was identified by X-ray diffractometer (XRD, Rigaku SmartLab, 9kW) with a diffraction angle (2θ) ranging from 10 to 70°. TEM images were obtained using a STEM (JEOL JEM-2100F) operated with a field emission gun at 200 kV. The samples were first dispersed in ethanol and drop-cast onto holey carbon-coated 400 mesh copper grids. The UV–vis diffuse reflectance spectroscopy was recorded using a UV–Vis spectrophotometer (Cary 4000) with ultrapure $BaSO_4$ as the reference. Raman spectra were obtained by a Raman spectrometer (Renishaw inVia) with the excitation wavelength of 785 nm at room temperature. XPS measurements were performed using a K-Alpha X-ray photoelectron spectrometer (Thermo Fisher Scientific, UK) with a monochromatic Al Kα X-ray source (excitation energy = 1,468.6 eV) and a base pressure of 3×10^{-9} Torr in the analytical chamber, and with an internal reference of C 1s at 284.0 eV. EPR measurements were performed on an EPR spectrometer (SPINSCAN X, ADANI) operating at 9.3 GHz (X band) using a 100 kHz field modulation. All the spectra were recorded at 298 K using a microwave power of 10 mW and accumulated for three times.

Electrochemical measurements.

All the measurements were performed on a CHI1030A electrochemical workstation. 4 mg catalyst and 200 μL 5 wt% Nafion solution were dispersed in 4 mL water/ethanol (3:1 v/v) by 10 min sonication to form homogeneous suspension. Then, 10 μL catalyst ink was drop-cast onto a glassy carbon electrode of 3 mm diameter (surface area = 7.07 mm^2) as the working electrode with a constant mass loading of 0.14 mg cm^{-2}. A linear sweep voltammogram from 0 to −0.6 V was measured at a scan rate of 1 mV s^{-1} in 0.5 M H_2SO_4 using a saturated calomel electrode and a Pt wire as the reference electrode and counter electrode, respectively. Pt/C (20 wt% platinum on graphitized carbon) is commercial available from Sigma-Aldrich. The Mott-Schottky plot was constructed based on the electrochemical data obtained using a typical three electrode system in phosphate buffer solution of pH 7.4. The Ag/AgCl (in 3 M NaCl solution) electrode and graphite were used as reference and counter electrode, respectively. The data were collected by

measuring the space-charge layer capacitance over a range of applied potentials (from −1.0 to 1.0 V) at 1,000 Hz using a CHI760E electrochemical station. The recorded potential was referenced to the reversible hydrogen electrode (RHE) according to the following equation: E (*vs*. RHE) = E (*vs*. Ag/AgCl) + 0.197 V + 0.0592 × pH.

Results and discussion

Monoclinic WO_3 nanoplate was first synthesized by directly annealing tungstic acid at 550 °C, which was afforded by a simple co-precipitation of sodium tungstate solution with HCl. To introduce disordered layer, the as-prepared WO_3 nanoplates were dispersed and stirred in Li-EDA solution[35] at room temperature for 4 h. During the Li-EDA treatment, a distinct color change from pale yellow to dark blue was observed (Figure 1a). The UV-vis diffusive reflectance spectra (UV-vis DRS, Figure 1b) reveal that the light response of Li-EDA treated WO_3 (LT-WO_3) has been extended, as evident from a significant absorption tail in the visible region (450 to 800 nm).

Such change in optical properties can arise from the oxygen vacancies created on the surface or modified crystal phase.[36, 37] X-ray diffraction (XRD) analysis was conducted to investigate the structural changes induced by Li-EDA treatment. As shown in Figure 1c, the XRD pattern of pristine WO_3 matches well with the monoclinic phase of WO_3 (JCPDS no. 43-1035) where the sharp diffraction peaks indicate its crystalline nature. LT-WO_3 also shows a similar pattern of diffraction peaks, indicating that the crystal structure is retained. However, the peaks are broader with much weaker intensities compared to those observed from pristine WO_3, suggesting reduced crystallinity due to the localized modification of crystal structure.[36]

Similar change was observed from the Raman spectra (Figure 1d), where the characteristic Raman peaks of WO_3 are broadened after the Li–EDA treatment. Two peaks at 273 and 326 cm^{-1}, which are assigned to the W^{6+}–O–W^{6+} bending vibration mode of bridging oxygen in WO_3 crystal lattice,[38] almost disappeared in LT-WO_3 spectrum, suggesting the partial removal of oxygen atoms. The peak at 716 cm^{-1} that is attributed to the long W^{6+}–O–W^{6+} bond stretching mode was also markedly reduced with a slight shift. In addition, the peak for the short W^{6+}–O–W^{6+} bond stretching at 808 cm^{-1} shows an appreciable broadening that is correlated to the weakening of W–O bond.[38] Furthermore, a small peak at 430 cm^{-1} appeared after the Li-EDA treatment indicates the presence of W species at lower oxidation states.[38-40] The reduction of W^{6+} to a lower oxidation state by Li-EDA is believed to weaken the W–O bond, which in turn leads to the partial loss of oxygen from the lattice. This is supported by the electron paramagnetic resonance (EPR) studies where only LT-WO_3 shows a signal at *g*-value of 2.002, an indication of oxygen vacancies (Figure 2).[14] Both Raman and EPR results are in good agreements with the observations from XRD measurements.

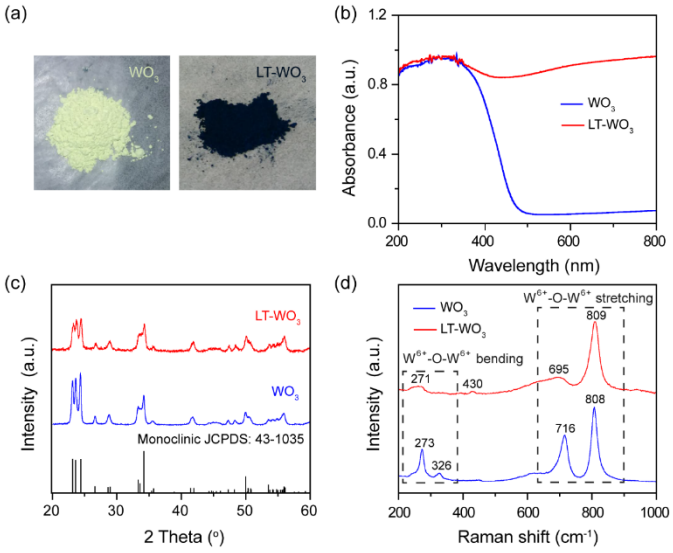

Figure 1. (a) Photographs of pristine WO_3 and LT-WO_3 obtained via Li–EDA treatment. (b) UV-vis diffusive reflectance spectra (UV-vis DRS) of WO_3 and LT-WO_3. (c) XRD and (d) Raman spectra of WO_3 and LT-WO_3.

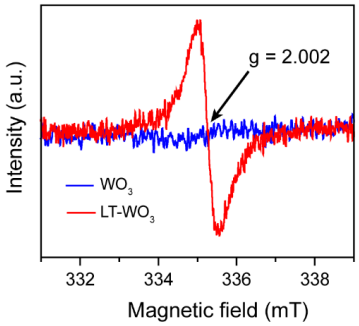

Figure 2. EPR spectra of WO_3 and LT-WO_3.

Figure 3 compares the transmission electron microscopic (TEM) images of as-prepared WO_3 and LT-WO_3 nanoplates. The typical morphology of WO_3 is a rectangular nanoplates (mean side length of *ca*. 130 nm) with some smaller nanoplates of irregular shapes (Figure 3a). A high resolution TEM (HR-TEM) image shown in Figure 3b clearly reveals well-ordered lattice fringes of 0.366 and 0.378 nm that can be indexed to the (200) and (020) planes of monoclinic phase WO_3, respectively. The corresponding selected area electron diffraction (SAED) pattern (inset in Figure 3b) shows the single-crystal spots that are in good agreements with the (200) and (020) planes. On the other hand, the TEM image of LT-WO_3 (Figure 3c) shows a similar but more round-shaped morphology with a slightly reduced average side length (*ca*. 77 nm). Moreover, from the HR-TEM (Figure 3d), thin disordered layer (average thickness = *ca*. 2 nm) is evident along the edge, which is supported by the disappearance of lattice fringes and its corresponding SAED pattern (inset in Figure 3d). The formation of disordered layer is attributed to the deprivation of surface lattice oxygen by solvated electrons during the treatment with Li–EDA, which is a strong reducing agent.[41] By reacting with Li-EDA, W^{6+} is reduced to a lower oxidation state, and oxygen atoms are removed from the surface lattice.[18, 35, 42] The removal of oxygen atoms would

lead to the crystal lattice deformation on the surface, leading to the decrease in both crystallinity and size of the nanoplates as observed from the XRD, TEM, and Raman spectroscopic studies.

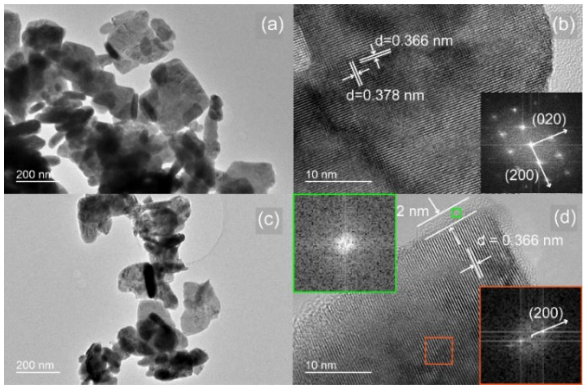

Figure 3. Electron microscopic analysis of WO_3 and LT-WO_3. (a) Low-resolution and (b) high-resolution TEM images of WO_3. (c) Low-resolution and (d) high-resolution TEM images of LT-WO_3. The insets in (b) and (d) show the FFT patterns of selected areas (orange squares: monoclinic phase core; green squares: disordered layer).

It is interesting that the core part of LT-WO_3 still retained the crystallinity as manifested by the clear lattice fringes (Figure 3d). We have conducted a series of time-resolved Li-EDA treatments to investigate the formation of disordered layer and control its thickness (Figure 4). The disordered layer starts to form on the edges after 2 h of reaction and gradually grows thicker with treatment time. The thickness of disordered layer reached up to 5 nm after 7 h, however, further prolonged reaction did not change the thickness, but only reduced the nanoplate size. The reaction between Li–EDA and WO_3 initially occurs at the Li–EDA/WO_3 interface. At early stage, solvated electrons can diffuse through thin disordered layer formed on the surface to reduce the W^{6+} ions in the inner crystal lattice. As the disordered layer becomes thicker, it acts as a passivation layer that hinders the diffusion of the electrons into the inner part. With further extended reaction time, the size of core shrinks, as the outer layer is lost. These results suggest that the surface disordered layer is closely associated with the formation of oxygen vacancies.

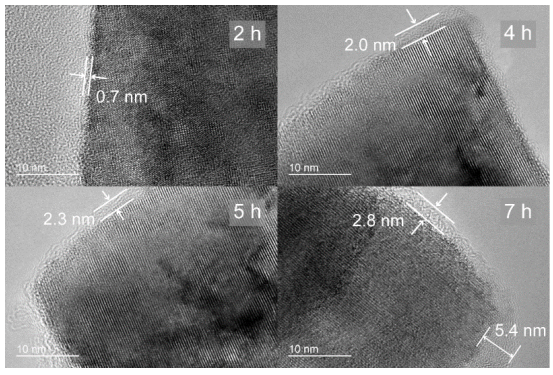

Figure 4. Time-resolved TEM analysis of the thickness of disordered layer in LT-WO_3 nanoplates treated for 2, 4, 5, and 7 h.

To confirm the formation of disordered layer, the surface species was characterized using X-ray photoelectron spectroscopy (XPS). Similar survey XPS spectra were obtained from pristine WO_3 and LT-WO_3, where only W and O were identified, with a small C 1s peak due to the adsorbed carbon-containing species, eliminating the possibility of Li contamination (binding energy of Li 1*s* is *ca*. 55.0 eV), especially in LT-WO_3 (Figure 5). From the normalized W 4*f* core level spectra (Figure 6a), only W^{6+} ions are detected in pristine WO_3, with the peaks at binding energy of 35.7 and 37.8 eV assigned to W $4f_{5/2}$ and W $4f_{7/2}$.[14] In contrast, the W 4*f* spectrum of LT-WO_3 shifts to a lower binding energy and becomes broader, indicates the presence of lower oxidation states. In addition to W^{6+} state, W^{5+} ions appear as a shoulder at binding energies of 34.5 and 36.4 eV. This is in good accordance with the Raman studies and further validates the reduction of W^{6+} to a lower oxidation state by Li-EDA. Additionally, a broad peak was seen from the O 1*s* spectrum of LT-WO_3 (Figure 6b), which can be deconvoluted into two peaks. The peak centered at 530.4 eV is ascribed to the lattice O^{2-} species (W–O–W),[14] while the other peak centered at 531.6 eV is assigned to O^{2-} in the vicinity of oxygen vacancies.[43] Meanwhile, the O 1*s* spectrum of pristine WO_3 shows a major peak for lattice oxygen atoms at 530.3 eV with a small peak at 531.6 eV, presumably due to the surface contamination during sample preparation. It is noted that both W 4*f* and O 1*s* peaks of LT-WO_3 exhibit binding energies slightly shifted to the lower values, *ca*. 0.2 and 0.1 eV, respectively. Similar shifts were observed from WO_3 after the chemical treatment as a result of the change in the electronic structure.[26, 44]

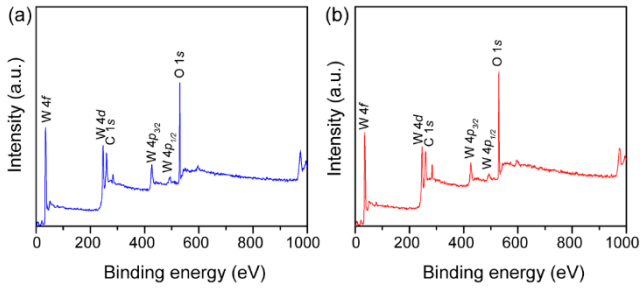

Figure 5. XPS survey spectra of (a) WO_3 and (b) LT-WO_3.

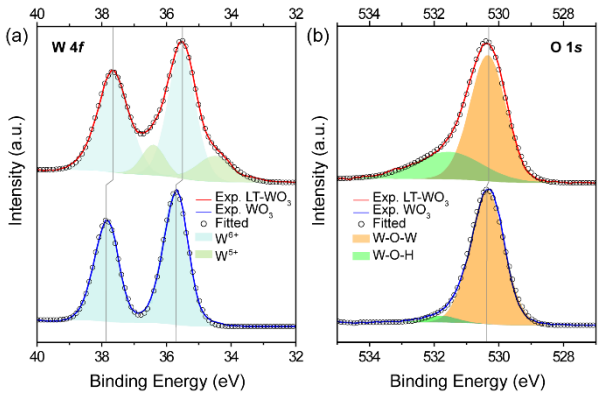

Figure 6. (a) W 4*f* and (b) O 1*s* XPS spectra of LT-WO_3 (top) and WO_3 (bottom).

Disordered atomic arrangement is known to affect the electronic structure, and thus physicochemical properties of

WO_3.[16, 25, 26] The observed change in the optical absorption of LT-WO_3 is related to the surface disordered layer. The band gap energies calculated by fitting the UV-vis DRS to Tauc equation are 2.68 and 2.74 eV for WO_3 and LT-WO_3, respectively (Figure S1). Despite the obvious color change, the optical band gap energies (E_g) did not show much difference. However, the valence band XPS (VB-XPS) spectra reveal the changes in the electronic structure and band offset (Figure 7a). The position of VB maximum (VBM) was first evaluated by linearly extrapolating the onset of XPS valence band spectra to the baseline, which reflects a band edge position with respect to the Fermi level (E_f). The VBM edge levels of WO_3 and LT-WO_3 were determined to be 2.63 and 2.43 eV, respectively, indicating the upshift of VBM by induced oxygen vacancies. Interestingly, the VB-XPS spectrum of LT-WO_3 also exhibits the VB tail state (1.31 eV with respect to E_f), suggesting the formation of additional electronic state. This mid-gap state would essentially broaden the VB width to create a reduced band gap (E_g' = 1.62 eV), and consequently allows the wider visible light absorption and change in sample color to dark blue.[45] We also engaged the Mott–Schottky plots to determine E_f levels and thus obtain the band structures of samples.[46, 47] Figure 7b shows the flat band potentials, which shifted from 0.5 to 0.25 V after Li-EDA treatment. The flat band potential reflects the difference between the E_f level and the water reduction potential of the sample. This shift of E_f confirms again that the surface disordered layer reconstructs the electronic structure of WO_3 by introducing oxygen vacancies. The formation of mid-gap is closely related to the disordered surface layer on LT-WO_3, which contains W^{5+} ions and oxygen vacancies (Figure 6). The self-doping of W^{5+} ions also modifies the electronic structure by creating a mid-gap and enhances the surface electron density, contributing to the upshift of the E_f.[16, 48, 49]

Combining the results from UV-Vis DRS, VB-XPS, and Mott–Schottky plot, we have constructed an energy level diagram qualitatively representing the changes in band structure of LT-WO_3, and presented in Figure 7c. The conduction band minimum (CBM) was estimated according to the equation of $E_{CBM} = E_{VBM} - E_g$. The upshift of the E_f induced by the disordered layer on LT-WO_3 caused the VBM shift from 3.13 to 2.68 V. With the E_g of 2.74 eV, the CBM in LT-WO_3 is determined to be −0.06 V, which satisfies the thermodynamic requirement for H_2 generation.

To verify this reformed band structure of LT-WO_3, we have carried out the photocatalytic HER using a mixed solution of Na_2S and Na_2SO_3 as a sacrificial agent under one sun illumination. LT-WO_3 indeed shows a remarkable performance in photocatalytic HER with the average rate of 94.2 μmol g^{-1} h^{-1} (Figure 8). The H_2 generation rate was stable during the continuous 25 h reaction, showing no discernable degradation in the catalytic activity. The control experiment conducted under the dark generated no detectable H_2. To the best of our knowledge, this is the first report of photocatalytic H_2 evolution from WO_3 without any co-catalysts. The creation of disordered surface layer on WO_3 is demonstrated to modify its electronic structure, thus endows a new capability of photocatalytic H_2 generation. It also seems to affect the generation and lifetime of charge carriers. The steady state photoluminescence (PL) spectra (Figure S2a) taken at room temperature show a much enhanced PL emission intensity, attributed to the higher concentration of photogenerated excitons. The time-resolved PL spectra (Figure S2b) indicates that the charge carriers in LT-WO_3 have more than 4 times longer lifetime (1.05 ± 0.05 ns) than those in WO_3 (0.25 ± 0.05 ns).

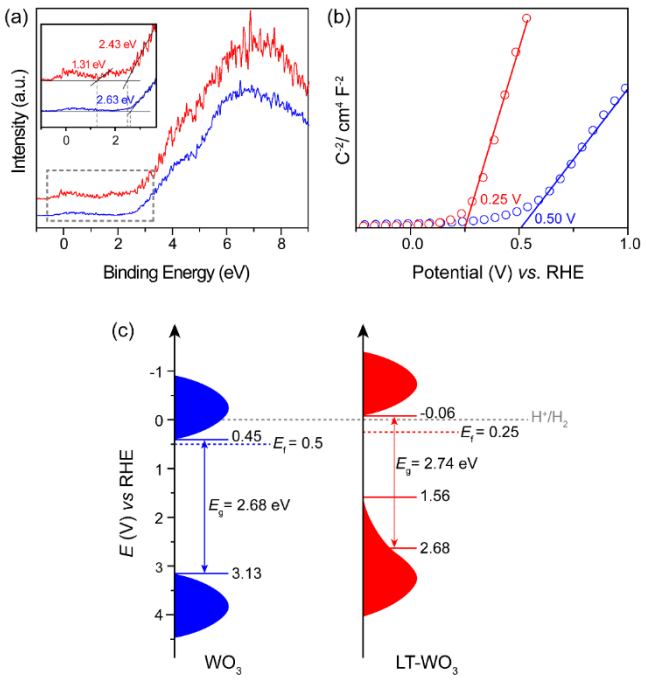

Figure 7. (a) VB-XPS and (b) Mott-Schottky plot of WO_3 and LT-WO_3. Inset in (a) is the enlarged area near the band edges indicated with a dotted box. (c) Schematic illustration of the energy levels of WO_3 and LT-WO_3 nanoplates.

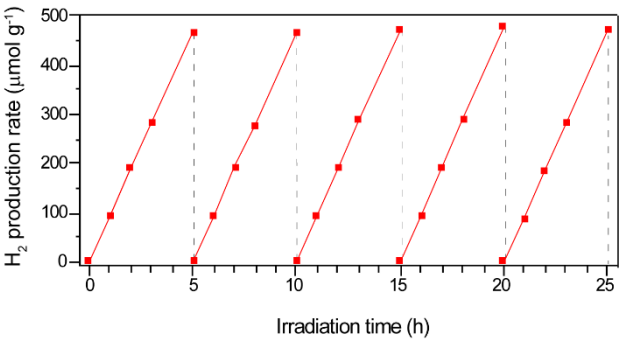

Figure 8. Photocatalytic H_2 production using LT-WO_3 as a photocatalyst for 25 h reaction of five cycles.

In order to gain further insight on the disordered surface layer of LT-WO_3, the surface reactivity was studied by examining the electrocatalytic activity in H_2 production. Figure 9a shows the polarization curves where the normalized current densities are plotted against applied potential without iR correction. LT-WO_3 shows a much lower overpotential (η) of −176 mV (*vs*. RHE, same below) at the current density of 10 mA cm^{-2} compared with pristine WO_3 (−667 mV). The corresponding Tafel slope of

LT-WO_3 is 59 mV dec^{-1} (Figure 9b), lower than that of WO_3 (88 mV dec^{-1}), implying its higher activities towards H_2 production. These results indicate that the disordered layer on WO_3 surface can significantly improve the surface reactivity towards H_2 production. The increased population of trapping sites for electron carriers (*i.e.*, oxygen vacancies) is believed to promote the electron transfer, which effectively reduces the energy barrier for proton reduction, and activates the surface reactivity towards H_2 production.[26, 27]

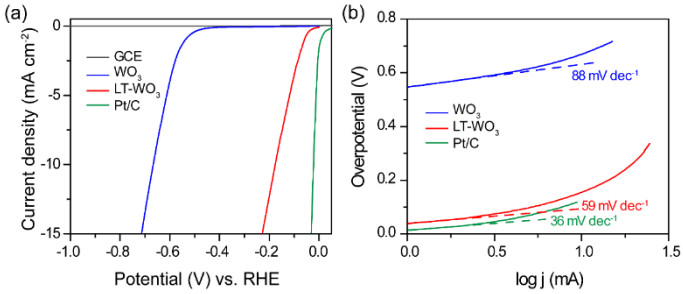

Figure 9. (a) Polarization curves and (b) Tafel plots of WO_3 and LT-WO_3 with Pt/C electrodes included for comparison.

Conclusions

In conclusion, the band structure of WO_3 has been successfully tuned by a simple surface defect engineering method, Li-EDA treatment. The formation of oxygen vacancies and self-doping of W^{5+} onto the surface of WO_3 through the generation of disordered surface layer create a mid-gap level in the electronic structure and shift the CBM above the H_2 reduction potential. This is the first example of tuning the band structure of WO_3 to realize co-catalyst-free photocatalytic H_2 evolution. Electrochemical investigations also reveal that the oxygen vacancy-rich disordered layer can provide efficient electron trapping sites that promote the surface activity for HER. Our work demonstrates the disordered layer on a semiconductor surface can be utilized to effectively tune the band structure and extend its catalytic applications.

Conflicts of interest

There are no conflicts to declare.

Acknowledgements

This work was supported by the Innovation and Technology Commission, The Hong Kong Polytechnic University (Grant No. G-YBSZ and 1-BE0Y), and the National Natural Science Foundation of China (Grants No. 21701135). LW acknowledged the award of a postdoctoral fellowship by The Hong Kong Polytechnic University. KYW acknowledged the support by the Patrick S.C. Poon endowed professorship.

Notes and references

1. T. Hisatomi, J. Kubota and K. Domen, *Chem. Soc. Rev.*, 2014, **43**, 7520-7535.
2. J. H. Montoya, L. C. Seitz, P. Chakthranont, A. Vojvodic, T. F. Jaramillo and J. K. Nørskov, *Nat. Mater.*, 2016, **16**, 70.
3. Y. Wang, H. Suzuki, J. Xie, O. Tomita, D. J. Martin, M. Higashi, D. Kong, R. Abe and J. Tang, *Chem. Rev.*, 2018, **118**, 5201-5241.
4. S. Fukuzumi, Y.-M. Lee and W. Nam, *Coord. Chem. Rev.*, 2018, **355**, 54-73.
5. E. Ha, L. Y. S. Lee, J. Wang, F. Li, K.-Y. Wong and S. C. E. Tsang, *Adv. Mater.*, 2014, **26**, 3496-3500.
6. J. Zhang, W. Yao, C. Huang, P. Shi and Q. Xu, *J. Mater. Chem. A*, 2017, **5**, 12513-12519.
7. W. Liu, E. Ha, L. Wang, L. Hu, L. Y. S. Lee and K.-Y. Wong, *Adv. Mater. Interfaces*, 2018, DOI: doi:10.1002/admi.201800611, 1800611.
8. I. Concina, Z. H. Ibupoto and A. Vomiero, *Adv. Energy Mater.*, 2017, **7**, 1700706.
9. G. Wang, Y. Yang, D. Han and Y. Li, *Nano Today*, 2017, **13**, 23-39.
10. P. Kofstad, *Phase Transit.*, 1996, **58**, 75-93.
11. J. Nowotny, M. A. Alim, T. Bak, M. A. Idris, M. Ionescu, K. Prince, M. Z. Sahdan, K. Sopian, M. A. Mat Teridi and W. Sigmund, *Chem. Soc. Rev.*, 2015, **44**, 8424-8442.
12. J. Jia, C. Qian, Y. Dong, Y. F. Li, H. Wang, M. Ghoussoub, K. T. Butler, A. Walsh and G. A. Ozin, *Chem. Soc. Rev.*, 2017, **46**, 4631-4644.
13. X. Pan, M.-Q. Yang, X. Fu, N. Zhang and Y.-J. Xu, *Nanoscale*, 2013, **5**, 3601-3614.
14. J. Meng, Q. Lin, T. Chen, X. Wei, J. Li and Z. Zhang, *Nanoscale*, 2018, **10**, 2908-2915.
15. Y. Yang, Y. Wang and S. Yin, *Appl. Surf. Sci.*, 2017, **420**, 399-406.
16. X. Chen, L. Liu, P. Y. Yu and S. S. Mao, *Science*, 2011, **331**, 746-750.
17. Y. Liu, Y. Li, S. Yang, Y. Lin, J. Zuo, H. Liang and F. Peng, *ChemSusChem*, 2018, DOI: doi:10.1002/cssc.201800940.
18. G. Yin, X. Huang, T. Chen, W. Zhao, Q. Bi, J. Xu, Y. Han and F. Huang, *ACS Catal.*, 2018, **8**, 1009-1017.
19. P. Yan, G. Liu, C. Ding, H. Han, J. Shi, Y. Gan and C. Li, *ACS Appl. Mater. Interfaces*, 2015, **7**, 3791-3796.
20. G. Wang, H. Wang, Y. Ling, Y. Tang, X. Yang, R. C. Fitzmorris, C. Wang, J. Z. Zhang and Y. Li, *Nano Lett.*, 2011, **11**, 3026-3033.
21. S. W. Kwon, M. Ma, M. J. Jeong, K. Zhang, S. J. Kim and J. H. Park, *Chem. Commun.*, 2016, **52**, 13807-13810.
22. Y. Cho, S. Kim, B. Park, C. L. Lee, J. K. Kim, K. S. Lee, I. Y. Choi, J. K. Kim, K. Zhang, S. H. Oh and J. H. Park, *Nano Lett*, 2018, **18**, 4257-4262.
23. S. Sun, T. Zhai, C. Liang, S. V. Savilov and H. Xia, *Nano Energy*, 2018, **45**, 390-397.
24. T. Xia, P. Wallenmeyer, A. Anderson, J. Murowchick, L. Liu and X. Chen, *RSC Adv.*, 2014, **4**, 41654-41658.
25. K. J. Kyu, C. Yoonjun, J. M. Jin, L.-W. Ben, S. Dongguen, Y. Yeonjin, W. D. Hwan, Z. Xiaolin and P. J. Hyeok, *ChemSusChem*, 2018, **11**, 933-940.
26. M. Ma, K. Zhang, P. Li, M. S. Jung, M. J. Jeong and J. H. Park, *Angew. Chem. Int. Ed.*, 2016, **55**, 11819-11823.
27. R. Zhang, F. Ning, S. Xu, L. Zhou, M. Shao and M. Wei, *Electrochim. Acta*, 2018, **274**, 217-223.
28. H. Zheng, Y. Tachibana and K. Kalantar-zadeh, *Langmuir*, 2010, **26**, 19148-19152.
29. S.-H. Lee, R. Deshpande, P. A. Parilla, K. M. Jones, B. To, A. H. Mahan and A. C. Dillon, *Adv. Mater.*, 2006, **18**, 763-766.
30. R. Xing, Y. Du, X. Zhao and X. Zhang, *Sensors*, 2017, **17**, 710.

31. X. Shi, I. Y. Choi, K. Zhang, J. Kwon, D. Y. Kim, J. K. Lee, S. H. Oh, J. K. Kim and J. H. Park, *Nat. Commun.*, 2014, **5**, 4775.
32. H. Zhen-Feng, S. Jiajia, P. Lun, Z. Xiangwen, W. Li and Z. Ji-Jun, *Adv. Mater.*, 2015, **27**, 5309-5327.
33. C. A. Bignozzi, S. Caramori, V. Cristino, R. Argazzi, L. Meda and A. Tacca, *Chem. Soc. Rev.*, 2013, **42**, 2228-2246.
34. Y. H. Li, P. F. Liu, L. F. Pan, H. F. Wang, Z. Z. Yang, L. R. Zheng, P. Hu, H. J. Zhao, L. Gu and H. G. Yang, *Nat. Commun.*, 2015, **6**, 8064.
35. K. Zhang, L. Wang, J. K. Kim, M. Ma, G. Veerappan, C.-L. Lee, K.-j. Kong, H. Lee and J. H. Park, *Energy Environ. Sci*, 2016, **9**, 499-503.
36. G. Wang, Y. Ling, H. Wang, X. Yang, C. Wang, J. Z. Zhang and Y. Li, *Energy Environ. Sci*, 2012, **5**.
37. J. Song, Z.-F. Huang, L. Pan, J.-J. Zou, X. Zhang and L. Wang, *ACS Catal.*, 2015, **5**, 6594-6599.
38. S. Bai, K. Zhang, L. Wang, J. Sun, R. Luo, D. Li and A. Chen, *J. Mater. Chem. A*, 2014, **2**, 7927-7934.
39. S.-H. Lee, H. M. Cheong, J.-G. Zhang, A. Mascarenhas, D. K. Benson and S. K. Deb, *Appl. Phys. Lett.*, 1999, **74**, 242-244.
40. W. Chun-Kai, D. R. Sahu, W. Sheng-Chang, L. Chung-Kwei and H. Jow-Lay, *J. Phys. D*, 2012, **45**, 225303.
41. R. S. Monson, in *Advanced Organic Synthesis*, ed. R. S. Monson, Academic Press, 1971, DOI: https://doi.org/10.1016/B978-0-12-504950-4.50006-X, pp. 25-30.
42. M. Ming, Z. Kan, L. Ping, J. M. Sun, J. M. Jin and P. J. Hyeok, *Angew. Chem. Int. Ed.*, 2016, **55**, 11819-11823.
43. Y. Sun, W. Wang, J. Qin, D. Zhao, B. Mao, Y. Xiao and M. Cao, *Electrochim. Acta*, 2016, **187**, 329-339.
44. H. Cheng, M. Klapproth, A. Sagaltchik, S. Li and A. Thomas, *J. Mater. Chem. A*, 2018, **6**, 2249-2256.
45. J. Liu, L. Han, N. An, L. Xing, H. Ma, L. Cheng, J. Yang and Q. Zhang, *Appl. Catal., B*, 2017, **202**, 642-652.
46. J. Liu, J. Ke, D. Li, H. Sun, P. Liang, X. Duan, W. Tian, M. O. Tadé, S. Liu and S. Wang, *ACS Appl. Mater. Interfaces*, 2017, **9**, 11678-11688.
47. L. Liao, Q. Zhang, Z. Su, Z. Zhao, Y. Wang, Y. Li, X. Lu, D. Wei, G. Feng, Q. Yu, X. Cai, J. Zhao, Z. Ren, H. Fang, F. Robles-Hernandez, S. Baldelli and J. Bao, *Nat. Nanotechnol*, 2013, **9**, 69.
48. F. Zuo, L. Wang, T. Wu, Z. Zhang, D. Borchardt and P. Feng, *J. Am. Chem. Soc.*, 2010, **132**, 11856-11857.
49. W. Huang, J. Wang, L. Bian, C. Zhao, D. Liu, C. Guo, B. Yang and W. Cao, *Phys. Chem. Chem. Phys.*, 2018, **20**, 17268-17278.